PHYSICAL REVIEW D **96,** 036002 (2017)

Padé approximants and analytic continuation of Euclidean Φ-derivable approximations

Gergely Markó[*]
Institute of Physics, Eötvös University, Pázmány Péter sétány 1/A, H-1117 Budapest, Hungary

Urko Reinosa[†]
Centre de Physique Théorique, École Polytechnique, CNRS, Université Paris-Saclay, F-91128 Palaiseau, France

Zsolt Szép[‡]
MTA-ELTE Statistical and Biological Physics Research Group, H-1117 Budapest, Hungary
(Received 27 June 2017; published 2 August 2017)

We investigate the Padé approximation method for the analytic continuation of numerical data and its ability to access, from the Euclidean propagator, both the spectral function and part of the physical information hidden in the second Riemann sheet. We test this method using various benchmarks at zero temperature: a simple perturbative approximation as well as the two-loop Φ-derivable approximation. The analytic continuation method is then applied to Euclidean data previously obtained in the $O(4)$ symmetric model (within a given renormalization scheme) to assess the difference between zero-momentum and pole masses, which is in general a difficult question to answer within nonperturbative approaches such as the Φ-derivable expansion scheme.

DOI: 10.1103/PhysRevD.96.036002

I. INTRODUCTION

In recent years, much progress has been achieved in accessing the properties of interacting quantum fields in equilibrium. Part of the success stems from the development of continuum nonperturbative tools [1–4] that allow to implement some of the resummations of perturbative diagrams that are required in this context. Most of these approaches are formulated in Euclidean space (or imaginary-time formalism) because, on general grounds, the equations are easier to solve than the corresponding ones in Minkowski space (or real-time formalism). For instance, to date, there is no complete Minkowski space study of the temperature driven symmetry restoration in the four-dimensional $O(N)$ model which could compete in precision with its Euclidean counterpart. Yet certain quantities of interest, such as transport coefficients, pole masses, and decay rates, require the use of the real-time formulation, and therefore a constant effort is put into extending the previous methods (not only formally but also at a computational level) to Minkowski space. In particular, the self-consistent scalar propagator equation was solved in Minkowski space at zero and finite temperatures, both in the symmetric and broken phases (see e.g. Refs. [5–11]). These spectral function-based numerical solutions were obtained in various nonperturbative approximations. More recently, the spectral function was accessed using an analytic continuation of the functional renormalization group (FRG) equations [12,13].

Another possible route toward real-time quantities is not to employ the above approaches directly in Minkowski space but rather to develop methods that allow for the analytic continuation of Euclidean data. A standard method used to extract the spectral function from Euclidean data employs Bayesian inference to invert the integral relation between Euclidean correlation functions and spectral functions. In order to overcome some difficulties of the maximal entropy method [14], a novel Bayesian method was developed recently in Ref. [15] and applied for example to extract spectral properties from bottomonium correlators [16] and solutions of the quark Dyson-Schwinger equation obtained in Landau gauge [17]. In the context of the Φ-derivable expansion scheme [also referred to as the two-particle irreducible (2PI) formalism], knowledge of the external propagator, which fully displays the (linear) symmetries of the theory, requires the resolution of a Bethe-Salpeter equation. Since the latter equation is more easily solved in Euclidean space (see for instance Ref. [18]), analytic continuation techniques are of great help in this case.

In this paper, we would like to investigate the analytic continuation method of Ref. [19] which constructs multipoint Padé approximants in the form of finite continued fractions. We test this method using various benchmarks. First, we consider the two-loop Φ-derivable approximation for a one-component scalar field at zero temperature for which Euclidean data are already available [20] and

[*]smarkovics@hotmail.com
[†]reinosa@cpht.polytechnique.fr
[‡]szepzs@achilles.elte.hu

Minkowski data are relatively easy to generate using dispersion techniques. Using this benchmark, we test to what extent the pole mass and more generally the spectral function determined directly in Minkowski space can be reproduced from the Euclidean solution. Our test shows also that we have some control on the choice of the appropriate analytic continuation (among the infinitely many possible choices). For a second test, we use simple one-loop perturbative formulas and investigate the ability of the continuation method to extract (physical) information hidden in the second Riemann sheet.

We then apply the Padé analytic continuation method on the previously obtained Euclidean space solution of Refs. [21,22] to assess how much pole masses differ from zero-momentum masses. A similar question was recently addressed in Ref. [23] in the context of the quark-meson model using the FRG approach. In our case, such a comparison is motivated by the fact that, in our previous Euclidean studies of the $O(4)$ model, the parametrization was done at $T = 0$ based, for simplicity, on the pion and sigma zero-momentum masses of the external propagator which are directly accessible from the effective potential in the imaginary-time formalism. Since a more correct parametrization should involve the corresponding pole masses, we would like to quantify how much the parametrization was distorted by the use of the zero-momentum masses. We mention also that, recently, the Padé analytic continuation method was applied in Ref. [24] to compute the pole mass of the internal propagator of the symmetry improved 2PI (SI2PI) formalism. In Ref. [25], we argued that, at least at two-loop order, the SI2PI formalism contains an inherent untamed infrared sensitivity in the broken phase, according to which the Euclidean propagator is not defined above some value of the volume of the system.[1] Here, we use the Padé analytic continuation method to investigate to what extent this IR sensitivity affects the pole mass of the corresponding Minkowski propagator.

The organization of the paper is as follows. In Sec. II, using dispersion techniques, we generate Minkowski data within the two-loop Φ-derivable approximation for a φ^4 model at zero temperature, with or without spontaneous symmetry breaking. In Sec. III, we present the multipoint Padé continuation method and perform various tests using both the Minkowski space solution of Sec. II and simple perturbative formulas. The continuation method is then used in Sec. IV to assess the difference between pole and zero-momentum masses in the context of the $O(4)$ model as well as the IR sensitivity of the pole mass in the two-loop SI2PI approximation. The conclusions of our study are presented in Sec. V, and some technicalities can be found in the Appendixes.

[1]This infrared sensitivity can be avoided for some specific (sharp) UV regulators. However, the specificity of these UV regulators makes this removal of the IR sensitivity artificial in a sense; see Ref. [25] for more details.

II. MINKOWSKIAN TWO-LOOP Φ-DERIVABLE APPROXIMATION IN THE φ^4 MODEL

In this section, we consider a relatively simple situation where the Φ-derivable equations can be solved directly and accurately in Minkowski space. The obtained results shall then be used as a benchmark for the Padé analytic continuation method to be presented in the next section. In what follows, $Q = (q_0, \vec{q})$ denotes a four-momentum in Minkowski space, and we introduce the notation

$$\int_Q \equiv \int_{-\infty}^{\infty} \frac{dq_0}{2\pi} \int \frac{dq^3}{(2\pi)^3}.$$

A. Generalities

The 2PI formalism typically gives access to a self-consistent equation for the two-point function of a given model, from which various observables can be determined, in principle. In contrast to the infinite tower of Dyson-Schwinger equations, the equation for the two-point function in the 2PI formalism is not coupled to higher n-point functions. The price to pay is, however, that the equation contains infinitely many terms coming from the loop expansion of the 2PI effective action, and then it needs to be truncated for any practical purpose. In the case of the φ^4 model, the two-loop truncation of the 2PI effective action leads to the following gap equation for the momentum dependent mass function $\bar{M}(Q)$ of the self-consistent propagator $\bar{G}(Q) \equiv i/(Q^2 - \bar{M}^2(Q) + i\epsilon)$ in the presence of an arbitrary field expectation value ϕ,

$$\bar{M}^2(Q) = m_0^2 + \frac{\lambda_2}{2}\phi^2 + \frac{\lambda_0}{2}\mathcal{T}[\bar{G}] + \frac{\lambda^2}{2}\phi^2\mathcal{I}[\bar{G}](Q), \quad (1)$$

where the tadpole and bubble integrals are defined respectively as

$$\mathcal{T}[G] \equiv \int_Q G(Q), \quad (2)$$

$$\mathcal{I}[G_1, G_2](K) \equiv -i\int_Q G_1(Q)G_2(Q+K), \quad (3)$$

with the shorthand notation $\mathcal{I}[G](K) \equiv \mathcal{I}[G, G](K)$. The physical value of the field ϕ, denoted $\bar{\phi}$, is given in terms of the field equation. In the two-loop order truncation, it reads

$$0 = \bar{\phi}\left(m_2^2 + \frac{\lambda_4}{6}\bar{\phi}^2 + \frac{\lambda_2}{2}\mathcal{T}[\bar{G}] + \frac{\lambda^2}{6}\mathcal{S}[\bar{G}]\right), \quad (4)$$

where the setting-sun integral at vanishing external four-momentum is defined as

$$\mathcal{S}[G_1,G_2,G_3] \equiv -i\int_Q\int_K G_1(Q)G_2(K)G_3(Q+K), \quad (5)$$

with a shorthand notation similar to that above, $\mathcal{S}[G] \equiv \mathcal{S}[G,G,G]$. Let us mention that the field equation may have multiple solutions. The solution $\bar{\phi}$ we are interested in is the one that minimizes the effective potential. The latter can also be computed within the 2PI formalism, but we shall not recall its expression here.

As discussed in Ref. [26], a total of five counterterms are needed in order to absorb the divergences present in Eqs. (1) and (4). These counterterms can be expressed in terms of two renormalized quantities, a mass parameter m^2 and a coupling λ, and a renormalization scale. Expanding the propagator around an auxiliary propagator $G_0(Q) = i/(Q^2 - M_0^2 + i\varepsilon)$, in which M_0 plays the role of the renormalization scale, the counterterms were explicitly determined in Ref. [27] and employed numerically in Ref. [20]. Similar counterterms, although determined at some fixed temperature in the symmetric phase, have been used in Refs. [9,21,22,28]. In the present study, we use the counterterms of Ref. [27], and in Appendix A, we show the formal relation between the renormalization method of Ref. [27] and that of Ref. [26], which is formulated in terms of various two-point and four-point functions. The explicitly finite gap and field equations obtained after renormalization are

$$\bar{M}^2(Q) = m^2 + \frac{\lambda}{2}(\phi^2 + \mathcal{T}_{\rm F}[\bar{G}]) + \frac{\lambda^2}{2}\phi^2\mathcal{I}_{\rm F}[\bar{G}](Q), \quad (6a)$$

$$0 = \bar{\phi}\left[m^2 + \frac{\lambda}{6}\bar{\phi}^2 + \frac{\lambda}{2}\mathcal{T}_{\rm F}[\bar{G}] + \frac{\lambda^2}{6}\mathcal{S}_{\rm F}[\bar{G}]\right]. \quad (6b)$$

The finite parts of the integrals, denoted by the subscript F, read

$$\mathcal{T}_{\rm F}[G] \equiv \int_Q G_{\rm r}(Q), \quad (7a)$$

$$\mathcal{I}_{\rm F}[G](Q) \equiv \mathcal{I}[G](Q) - \mathcal{I}[G_0], \quad (7b)$$

$$\mathcal{S}_{\rm F}[G] \equiv \mathcal{S}[\delta G] + 3\mathcal{S}[\delta G,\delta G,G_0] + 3\int_Q G_{\rm r}(Q)\mathcal{I}_{\rm F}[G_0](Q), \quad (7c)$$

where $\mathcal{I}[G_0] \equiv \mathcal{I}[G_0](Q=0)$ and, as a result of expanding G around G_0, one has

$$\delta G(Q) = G(Q) - G_0(Q), \quad (8a)$$

$$G_{\rm r}(Q) = \delta G(Q) - i\left(M_0^2 - M_1^2 - \frac{\lambda^2}{2}\phi^2\mathcal{I}_{\rm F}[G_0](Q)\right)G_0^2(Q), \quad (8b)$$

with $M_1^2 \equiv m^2 + \frac{\lambda^2}{2}(\phi^2 + \mathcal{T}_{\rm F}[G])$. Each of the three terms on the rhs of Eq. (7c) is UV finite.

B. Use of dispersion relations

To put the system (6) in a convenient form in view of its numerical resolution, we now make use of dispersion relations. We first focus on the momentum dependent bubble integral $\mathcal{I}_{\rm F}[G](K)$. A standard method for dealing with such an integral in Minkowski space is to use the spectral representation for the propagator and a subtracted dispersion relation (see e.g. Ref. [29]) relating the real and imaginary parts of the integral. The spectral representation for the propagator is

$$G(Q) = \int_0^\infty \frac{ds}{2\pi}\frac{i\rho(s)}{Q^2 - s + i\varepsilon}, \quad (9)$$

with the spectral function defined as the (real) function $\rho(Q^2) = 2\Im[iG(Q)]$. In the two-loop approximation considered here, the leading contribution to the propagator at large Q is entirely given by the tree-level term, $G(Q) \sim i/Q^2$. It then follows from Eq. (9) that the spectral function obeys the following sum rule[2]:

$$\int_0^\infty \frac{ds}{2\pi}\rho(s) = 1. \quad (10)$$

We note also that $\rho(s) \sim 1/s^2$ at large s in the approximation at hand (if $\bar{\phi} \neq 0$).

Using Eq. (9) in a particular integral containing the self-consistent propagator is helpful because the integral over the momentum becomes perturbative and can be carried out using standard techniques, yielding an integral kernel in the rewritten expression of the original integral. In particular, we can use this rewriting in order to evaluate the imaginary part of the bubble integral $\mathcal{I}_{\rm F}[G](Q)$. Using Eq. (9) in the integral for $\mathcal{I}[G](Q)$, carrying out the momentum integration, and taking the imaginary part, while noting that $\Im\mathcal{I}_{\rm F}[G](Q) = \Im\mathcal{I}[G](Q)$, one obtains

$$\Im\mathcal{I}_{\rm F}[G](Q) = \int_0^\infty \frac{ds_1}{2\pi}\int_0^\infty \frac{ds_2}{2\pi}\rho(s_1)\rho(s_2)\Im\mathcal{I}_0[G_1,G_2](Q), \quad (11)$$

where $G_j(Q) = i/(Q^2 - s_j + i\varepsilon)$, $j = 1, 2$. The UV finite kernel $\Im\mathcal{I}_0[G_1,G_2](q)$ is the imaginary part of the perturbative bubble with mass squares s_1 and s_2. It is given in terms of the Källén function $\lambda(x,y,z) = (x-y-z)^2 - 4yz$ as

[2]This relation still holds beyond the present approximation for the spectral function associated with the bare propagator, in the presence of an ultraviolet regulator. It needs to be modified by a renormalization factor for the spectral function associated to the renormalized propagator.

$$\Im\mathcal{I}_0[G_1,G_2](Q) = -\frac{\sqrt{\lambda(Q^2,s_1,s_2)}}{16\pi Q^2} \times \Theta(Q^2-(\sqrt{s_1}+\sqrt{s_2})^2), \quad (12)$$

with $\Theta(x)$ being the Heaviside step function.

We could obtain the real part of $\mathcal{I}_F[G](Q)$ in the same fashion. It is, however, more efficient to make use of the dispersion relation that connects it to its imaginary part. Since the real part of the finite bubble integral grows logarithmically in the approximation at hand, we need a once-subtracted dispersion relation (see Appendix B for more details),

$$\Re\mathcal{I}_F[G](\sqrt{s}) = \mathcal{I}_F[G] + \frac{s}{\pi}\mathcal{P}\int_0^\infty ds' \frac{\Im\mathcal{I}[G](\sqrt{s'})}{s'(s'-s)}, \quad (13)$$

where we have again used that $\Im\mathcal{I}_F[G](Q) = \Im\mathcal{I}[G](Q)$ as well as $\Re\mathcal{I}_F[G] = \mathcal{I}_F[G]$, with our notational convention $\mathcal{I}[G] = \mathcal{I}[G](Q\equiv 0)$. Each term in the previous relation is finite. The subtracted piece $\mathcal{I}_F[G]$ can be conveniently computed using Eq. (9) for G. We find

$$\mathcal{I}_F[G] = \int_0^\infty \frac{ds_1}{2\pi}\int_0^\infty \frac{ds_2}{2\pi}\rho(s_1)\rho(s_2)\mathcal{I}_0[G_1,G_2] - \mathcal{I}[G_0] = \int_0^\infty \frac{ds_1}{2\pi}\int_0^\infty \frac{ds_2}{2\pi}\rho(s_1)\rho(s_2)\mathcal{I}_{0,F}[G_1,G_2], \quad (14)$$

where $\mathcal{I}_{0,F}[G_1,G_2] = \mathcal{I}_0[G_1,G_2] - \mathcal{I}[G_0]$ and we have used the sum rule (10) to bring $\mathcal{I}[G_0]$ under the integral. The difference $\mathcal{I}_{0,F}[G_1,G_2]$ of pertubative bubble integrals is UV finite. It can then be computed in any regularization scheme, with the result

$$\mathcal{I}_{0,F}[G_1,G_2] = \frac{(s_1-s_2)^{-1}}{16\pi^2}\left(s_1\ln\frac{s_1}{eM_0^2} - s_2\ln\frac{s_2}{eM_0^2}\right). \quad (15)$$

We now turn our attention to the principal value integral appearing in Eq. (13). Since this integral depends on which interval the imaginary part of the bubble has a support, we have to say a few words on the form of the spectral function. In the present article, we restrict ourselves to spectral functions which have a singular part, corresponding to a real pole of the propagator. In this case, one can write

$$\rho(s) = 2\pi Z\delta(s-\bar{M}_p^2) + \sigma(s), \quad (16)$$

where the continuum part $\sigma(s)$, starting at the two-particle threshold, is given in Eq. (B7) and the pole mass $\bar{M}_p$ is defined as $\bar{G}^{-1}(Q=\bar{M}_p)=0$ or, equivalently, in terms of the gap mass $\bar{M}^2(Q)$, as

$$\bar{M}_p^2 = \bar{M}^2(\bar{M}_p^2). \quad (17)$$

Using that the imaginary part of the bubble integral, along with σ, is nonzero only for $s > s_{th} = 4\bar{M}_p^2$, one can write the real part of the finite bubble integral in the form

$$\Re\mathcal{I}_F[G](\sqrt{s}) = \mathcal{I}_F[G] + \frac{s}{\pi}\mathcal{P}\int_{s_{th}}^\infty ds' \frac{\Im\mathcal{I}[G](\sqrt{s'})}{s'(s'-s)}, \quad (18)$$

with $\mathcal{I}_F[G]$ given in (14).

Finally, we discuss the evaluation of the finite tadpole and setting-sun integrals $\mathcal{T}_F[G]$ and $\mathcal{S}_F[G]$ defined in (7a) and (7c). The simplest way to compute them is by using the Euclidean propagator obtained through analytic continuation from (9) as

$$G_E(Q_E) = \int_0^\infty \frac{ds}{2\pi}\frac{\rho(s)}{Q_E^2+s}. \quad (19)$$

For instance, the unsubtracted tadpole $\mathcal{T}[G]$ that enters $\mathcal{T}_F[G]$ can be written, owing to a Wick rotation, as $\mathcal{T}[G] = \int_{Q_E} G_E(Q_E) \equiv \mathcal{T}_E[G_E]$. Similarly, one finds $\mathcal{S}[G] = -\int_{Q_E}\int_{K_E} G_E(Q)G_E(K)G_E(Q+K) \equiv -\mathcal{S}_E[G_E]$. With the Euclidean version of (8), $\mathcal{T}_F[G]$ and $\mathcal{S}_F[G]$ are then evaluated with an appropriate numerical cutoff.

C. Results

The iterative numerical algorithm for the resolution of the system (6) is described in detail in Appendix C. Here, we concentrate on describing the results obtained in the broken symmetry phase of the model. We explore in Sec. II C 2 the region of the parameter space (m^2,λ) where such a type of solution exists. All dimensionful quantities are measured in units of M_0 throughout this paper, that is, in the numerical code $M_0 = 1$.

1. Minkowskian solution

A typical broken phase solution of the gap and field Eqs. (6) can be seen in Fig. 1: the left panel shows the real and imaginary parts of the self-energy, while the right panel shows the pole and the continuum parts of the corresponding spectral function. We compare these quantities to perturbative ones obtained using a tree-level spectral function $\rho(Q) = 2\pi\delta(Q^2-M^2)$ to evaluate the integrals, with $M^2 \equiv \bar{M}^2(Q=0)$. We see that, even for a relatively large value of the coupling, the 2PI self-energy is not much different from a perturbative one. This is due to the fact that in the two-loop approximation the momentum dependence of the self-energy is logarithmic and that the mass $M^2 \equiv \bar{M}^2(Q=0))$ is then very close to $\bar{M}_p^2$. Note, however, that resummation of a perturbative series is needed in order to know the value of M^2; hence, the comparison tells us that

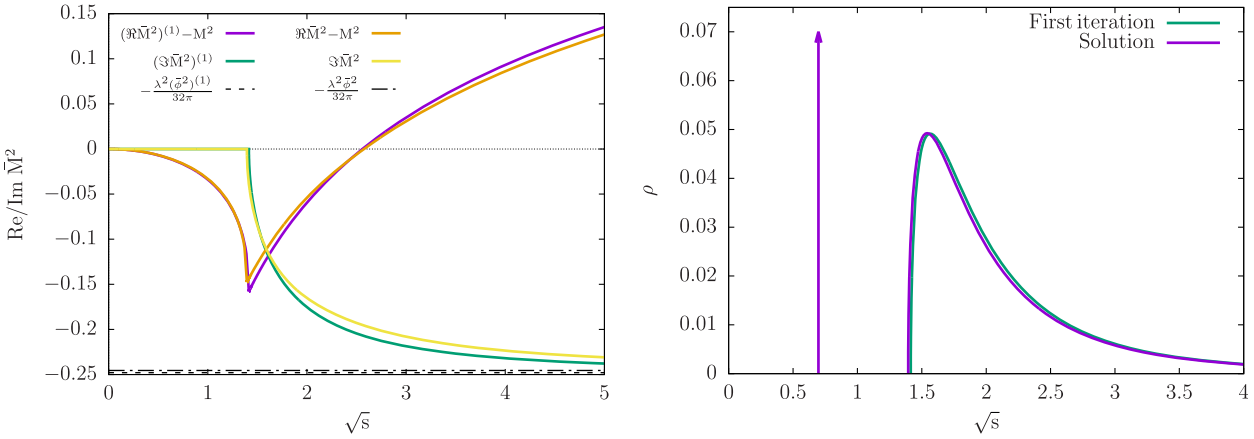

FIG. 1. Left panel: real and imaginary parts of the self-energy for a broken phase solution with $\lambda = 15$ and $m^2 = -0.28666$ obtained by solving (6) and characterized by $\bar{M}^2(Q=0) \equiv M^2 = 0.5$, $\bar{M}^2_{\rm p} = 0.4862$, $\bar{\phi} = 0.3312$, and $Z = 0.96904$, compared with a perturbative expression evaluated with a mass squared equal to $\bar{M}^2(Q=0)$ and a field value $\bar{\phi}^{(1)} = -0.3328$, obtained in the first iteration [in the plot, the value of the field is illustrated by the value of the limit $\Im\bar{M}^2(Q\to\infty)$]. Right panel: the spectral functions corresponding to the first iteration and to the solution of the 2PI equations.

the momentum dependence of the self-energy is similar to a perturbative one.[3]

2. Parametrization

In previous studies [28,30], we analyzed the parameter space of the model at $T = 0$ and how it was divided into regions corresponding to systems that displayed a symmetric phase and systems that displayed a broken phase. In those studies, the renormalization was carried out in the symmetric phase at a large enough fixed temperature $T_\star$ that played the role of the renormalization scale. It is interesting to see how this discussion appears in the present scheme where the renormalization is performed directly at $T = 0$, where the parameters m^2 and λ do not have the same meaning as in previous studies and where the role of the renormalization scale is played by M_0 rather than $T_\star$.

Apart from the occurrence of the above-mentioned two regions of the parameter space, the detailed investigation of Ref. [22] shows that, within a given 2PI approximation, one could have physical and unphysical branches of solutions to the gap equation (as ϕ is varied), which could merge for some values of the field. In this case, there is a region of ϕ where the gap equation admits no solution. This could result in the absence of a solution to the coupled system of gap and field equations if the would-be $\bar{\phi}$ were to be engulfed by the region of ϕ over which the gap equation has no solution. We have shown in Ref. [22] that a localized approximation to the momentum dependent gap mass is useful to investigate the loss of solution. We now show that an unphysical solution to the full 2PI equations can indeed be found. However, for the sake of simplicity, we use the localized approximation introduced in Ref. [22] to find the region of parameters where a loss of solution happens.

Our analysis reveals the existence of three curves which, as shown in the left panel of Fig. 2, delimit different regions of the (m^2, λ) parameter space. The physically most relevant one, denoted $\lambda_{\rm c}(m^2)$, separates the region where only a symmetric phase exists from the region where there is potentially a broken phase solution. This curve is a critical line in the parameter space, in the sense that, for these parameters, the physical solution is at $\bar{\phi} = 0$ with no $\bar{\phi} \neq 0$ solution and the curvature of the potential at $\phi = 0$ is vanishing. The condition of vanishing curvature thus defines the $\lambda_{\rm c}(m^2)$ curve through the relation

$$m^2 + \frac{\lambda_{\rm c}}{2}\mathcal{T}_{\rm F}[\bar{G}_{\phi=0}] + \frac{\lambda_{\rm c}^2}{6}\mathcal{S}_{\rm F}[\bar{G}_{\phi=0}] = 0. \tag{20}$$

The second line, denoted $\lambda_-(m^2)$, delimits the region where a loss of solution occurs from the region where the coupled gap and field equations do admit a solution. We expect such a region based on our previous investigations in Ref. [22]. For an example, the left panel of Fig. 2 shows a value of the coupling ($\lambda = 34$) at which the solution is lost for $m^2 < -0.12$, while for $m^2 > -0.12$, $\bar{M}^2_{\bar{\phi}\neq 0}(m^2)$ is multivalued. Multivaluedness is usually the signal of the appearance of unphysical branches, which can collide with the physical branch and lead to a loss of solution. In our case, the physical branch is always the upper one. This branch continuously connects to the $\phi = 0$ solution (in the case of parameters where the solution exists for any $\phi \geq 0$), where the unphysical branch disappears and only the physical

[3]Another possibility is to parameterize the system directly in terms of M^2, with, however, the important subtlety that two physically distinct systems (one in the broken phase and one in the symmetric phase) can lead to the same parameters (M^2, λ); see the discussion in Appendix C.

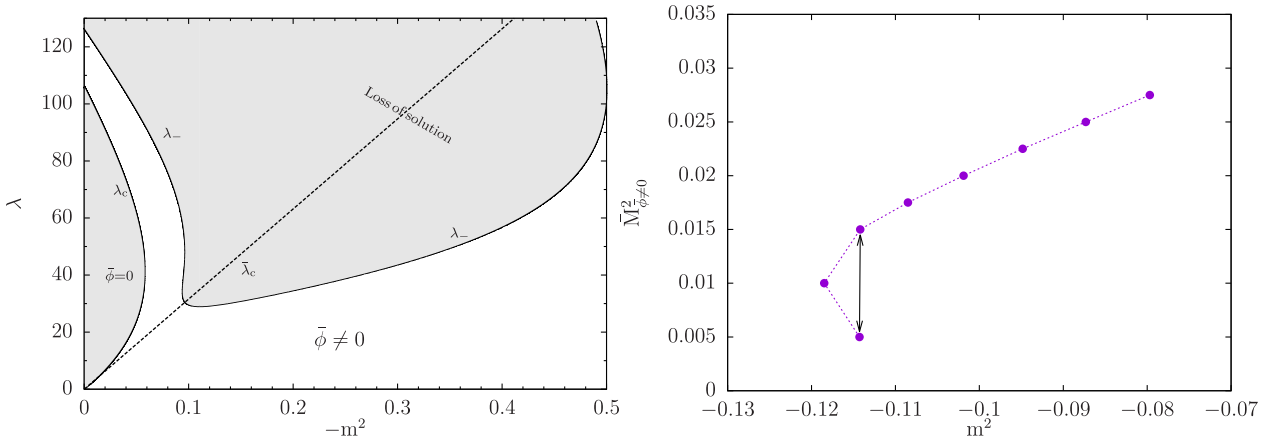

FIG. 2. Left panel: the parameter space in the localized approximation. The λ_c and $\bar{\lambda}_c$ curves coincide with the ones of the full 2PI case, while λ_- represents an approximation to the boundary of the region where a loss of solution is observed in the full 2PI case. Right panel: the gap mass of the broken phase solution $\bar{M}^2_{\bar{\phi}\neq 0}$ as a function of the renormalized mass parameter m^2. The results are obtained at a fixed $\lambda = 34$ using the M^2 parametrization discussed in Appendix C. The fact that the curve is multivalued in some m^2 range signals the appearance of an unphysical solution (lower branch) there. At this value of the coupling, the loss of solution occurs in the region $m^2 < -0.12$.

solution remains.[4] It is important to note here that, in order to find the unphysical branch of the solution, it was very helpful to reparametrize our equations in terms of the local part of the self-energy $\bar{M}^2(Q=0)$, rather than m^2, as explained in Appendix C around (C2). For further details on unphysical branches of solutions and the loss of solution, we direct the reader to Ref. [22]. In principle, the $\lambda_-(m^2)$ curve can be obtained in the full 2PI case by searching, at each value of m^2, for the value of the coupling where a loss of solution to the coupled equations occurs, as shown in the right panel of Fig. 2. Since this is a tedious procedure, as for large λ the convergence of the iterations is slow and strongly initial condition dependent, we resort to the much simpler localized approximation used in Refs. [22,31,32], which qualitatively reproduces the solution of the full 2PI equations. In this approximation, the full self-energy is replaced by its zero-momentum value resulting in a tree-level type propagator with a self-consistent mass. Finally, we define $\bar{\lambda}_c(m^2)$ as the curve where the gap mass at $\phi = 0$ vanishes. For $\lambda < \bar{\lambda}_c$, the gap equation admits no solution at $\phi = 0$, which also makes the potential unreachable there. Using the gap Eq. (6a) at $\phi = 0$ and that $\mathcal{T}_F[\bar{G}]|_{\bar{M}^2=0} = M_0^2/(16\pi^2)$, one can easily see that $\bar{\lambda}_c(m^2) = -32\pi^2 m^2/M_0^2$.

III. ANALYTIC CONTINUATION OF EUCLIDEAN SOLUTIONS USING PADÉ APPROXIMANTS

In this section, we would like to use Padé approximants in order to analytically continue functions known only at a finite number of points in the complex plane. We employ the multipoint Padé approximant (see Refs. [19] and [33]) calculated for a function known at N complex points z_i, $f(z_i) = u_i$, $i = 1\ldots,N$, using a finite continued fraction. Using the notation $\frac{1}{1+}x \equiv \frac{1}{1+x}$, the finite continued fraction is written in the form

$$C_N(z) = \frac{a_1}{1+}\frac{a_2(z-z_i)}{1+}\cdots\frac{a_N(z-z_{N-1})}{1}, \qquad (21)$$

and the task is to determine its N coefficients a_i from the conditions $C_N(z_i) = u_i$. An elegant and efficient way to achieve this is by recursion: the coefficients are obtained as $a_i = g_i(z_i)$, by defining[5]

$$g_1(z_i) = u_i, \qquad i = 1,\ldots,N, \qquad (22a)$$

$$g_p(z) = \frac{g_{p-1}(z_{p-1}) - g_{p-1}(z)}{(z-z_{p-1})g_{p-1}}, \qquad p \geq 2. \qquad (22b)$$

Working out explicitly the condition $a_i = g_i(z_i)$ for a few values of i, one sees that basically one needs to construct a triangular matrix $t_{i,j}$ using the recursion $t_{i,j} = (t_{i-1,i-1}/t_{i-1,j} - 1)/(z_j - z_{i-1})$, for $j = 2,\ldots,N$ and $i = 2,\ldots,j$, starting from its first row $t_{1,j} = u_j$, $j = 1,\ldots,N$.

The finite continued fraction can be written as a rational function, $C_N(z) = A(z)/B(z)$, which we do not give here because we do not use that form. We only mention that the polynomials $A(z)$ and $B(z)$ are both of order $(N-1)/2$ for N odd and of order $(N-2)/2$ and $N/2$, respectively,

[4] Actually, at all ϕ, including the vanishing field limit, there exists yet another unphysical branch, where the gap mass is exponentially large. We disregard this solution of the gap equation when discussing physical and unphysical branches.

[5] In the second relation, it is understood that z is part of the set of discrete points z_i.

for N even. This means that with increasing N two Padé sequences of the type $P_k^k(z)$ (for $N = 2k+1, k \geq 0$) and $P_{k+1}^k(z)$ (for $N = 2(k+1), k \geq 0$) are generated. When all the continued fraction coefficients are non-negative, it is known (see Ref. [34]) that $P_k^k(z)$ decreases, while $P_{k+1}^k(z)$ increases monotonically with k. The first sequence has a lower bound, while the second sequence has an upper bound which for $k \to \infty$ is a Stieltjes function $F(z)$, that is, a function of the form $F(z) = \int_0^\infty dt\rho(t)/(1+zt)$, with $\rho(t) \geq 0$ in the domain of integration.

We shall use the above method to obtain the propagator $\bar{G}(Q)$ for $Q^2 > 0$, from the knowledge of the same propagator at a finite number of negative $Q^2 = -Q_{\rm E}^2$ values in the Euclidean domain. In practice, we fix $\vec{q}$ (to zero in our case) and define the original Padé approximant as a function of the Matsubara frequency ω_n, and, to carry out the analytic continuation, we evaluate it at $\omega_n = -i\omega + \varepsilon$, where the $\varepsilon \to 0$ limit can be safely taken. We should of course keep in mind that the analytic continuation of a finite number of data is not unique and leads to various solutions that differ by their asymptotic behaviors as $|z| \to \infty$.[6] The ability of the method to reproduce the expected propagator then needs to be tested, and we will do so by using the explicit Minkowskian solution obtained in the previous section. Another subtle point is that, by definition, the Padé approximant has no branch cut and thus there is only one Riemann sheet to be considered. It is then a question of how the method can allow us to access physical information usually hidden in the second Riemann sheet of the propagator. A related issue is the fact that the Padé approximant does not obey the Schwarz reflection property, whereas the analytic propagator (B2) obeys this property [$\mathcal{G}(s^*)^* = -\mathcal{G}(s)$ with our conventions] in the first Riemann sheet, as is easily checked.

A. Test I: Ability to access the spectral function

To test the quality of the Padé analytic continuation, we use two test functions: the Euclidean 2PI self-energy extracted from Eq. (19) using the spectral function obtained as the solution of (6) and the zero temperature finite perturbative Euclidean bubble with square mass $M^2 = 0.5$:

$$\mathcal{B}_{0,\rm F}[G_M](Q_{\rm E}) = \frac{1}{16\pi^2}\left(2 - \log\frac{M^2}{M_0^2} + \sqrt{1+\frac{4M^2}{Q_{\rm E}^2}}\log\frac{\sqrt{1+\frac{4M^2}{Q_{\rm E}^2}}-1}{\sqrt{1+\frac{4M^2}{Q_{\rm E}^2}}+1}\right). \tag{23}$$

[6]Knowing some data $d_1, \ldots, d_n$ for a finite set of points $z_1, \ldots, z_n$ and given an analytic continuation $f(z)$ of these data, which is such that $f(z_i) = d_i$, we can construct another analytic continuation of the same data as, for instance, $g(z) = f(z) + \prod_{j=1}^n (\exp\{i2\pi z/z_j\} - 1)$.

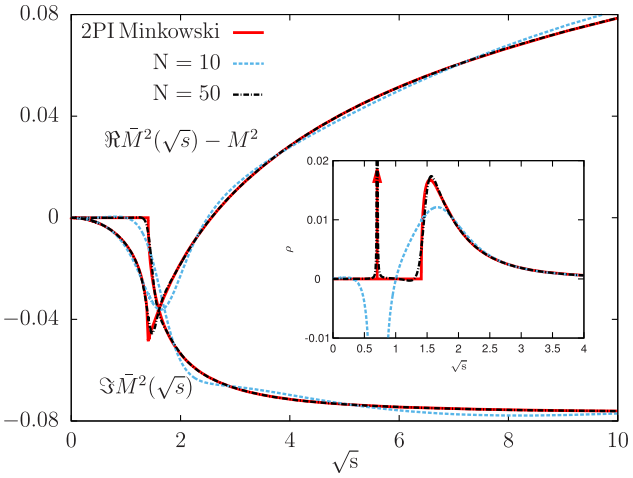

FIG. 3. The real and the imaginary parts of the analytically continued Euclidean 2PI self-energy given by (19) are compared to the corresponding quantities computed directly in Minkowski space from (6). The inset shows the same comparison for the spectral function. For Padé analytic continuation, we used $N = 10$ and $N = 50$ points in the $[0, 10M]$ interval of Euclidean momentum.

In both cases, we compare the real and imaginary parts of the analytically continued quantity to the one computed in the Minkowski space, which in the latter case is $\bar{M}^2(Q)$. For the comparison in the 2PI case, we use the parameters $m^2 = -0.2611$ and $\lambda = 5$, for which one obtains $M^2 \equiv \bar{M}^2(Q=0) = 0.5$ and $\bar{\phi} = 0.5566$. These agree with the values obtained with the numerical code used in Ref. [20] to solve the Euclidean version of the model in the present renormalization scheme.

In Fig. 3, we show the Padé analytically continued real and imaginary parts of the Euclidean 2PI self-energy and the corresponding spectral function compared to the quantities computed directly in Minkowski space. We see that, while using $N = 10$ points in (21) leads to a noticeable error almost everywhere, except for the real part of the self-energy at small $\sqrt{s}$, the multipoint Padé approximation using $N = 50$ points has difficulties reproducing the Minkowski result only in a narrow neighborhood of the threshold. However, even with $N = 10$ points, the analytical continuation gives a good approximation for the pole mass, $\bar{M}_{\rm p} = 0.70387$, compared to the value $\bar{M}_{\rm p} = 0.70392$ obtained from a direct calculation. Based on this observation, we can trust our results presented in Sec. IV concerning the comparison of zero-momentum and pole masses.

In order to quantify the quality of the analytic continuation over a significant region of momentum, we define the following Minkowski space integral,

$$\mathcal{Q} = \int_{\sqrt{s}_{\rm min}}^{\sqrt{s}_{\rm max}} dq (F(q) - \mathcal{F}(q))^2, \tag{24}$$

where F is the original function and $\mathcal{F}$ is its approximation obtained using analytic continuation, and with $\sqrt{s}_{\rm min\,/\,max}$

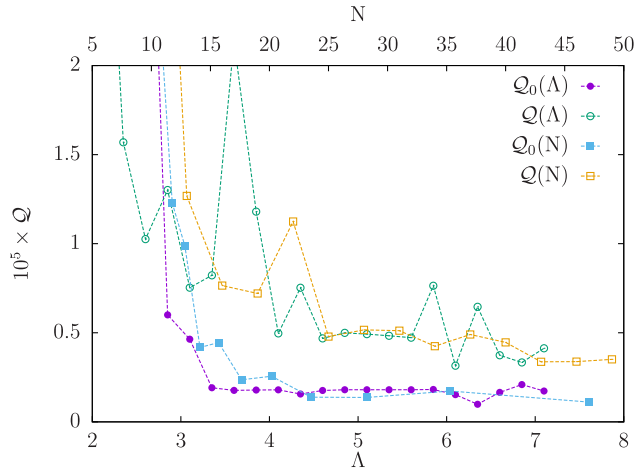

FIG. 4. The quality of the Padé analytic continuation of the Euclidean perturbative bubble ($\mathcal{Q}_0$, filled symbols) and the Euclidean self-energy ($\mathcal{Q}$, empty symbols). The circle symbols correspond to the bottom x axis and were obtained using a fixed number of sampling points ($N = 50$) in an interval with variable upper limit Λ, while the square symbols correspond to the top x axis and were obtained using N sampling points in a fixed width interval with upper limit $\Lambda = 10$.

chosen appropriately. In Fig. 4, we show this quantity $\mathcal{Q}$ as a function of the sampled region with fixed sampling frequency (bottom x axis) and as a function of the number of sample points on fixed region (top x axis). We see convergence both by increasing the sampled region and by increasing the number of points. While a perfect continuation would mean $\mathcal{Q} = 0$, the curves do not tend to zero, which we attribute to the error arising from finite number representation and the inherent differences in the analytic properties of the approximated functions and the Padé approximants. Also note that the combined results have some implications on the continuation of finite temperature data. The results corresponding to the bottom axis tell us that, at a certain temperature, there is a limiting Matsubara frequency, over which including new frequencies does not improve the quality of the continuation. At the same time, the results associated to the top axis indicate that with fewer frequencies in the relevant range, i.e. by increasing the temperature, the quality of the continuation deteriorates.

B. Test II: Ability to access physical information in the second Riemann sheet

We show now that the Padé analytic continuation of Euclidean data is capable of finding physically relevant complex poles in the case of an $O(4)$ symmetric model. Since we have 2PI results in Minkowski space only in the one-component case, we use as a benchmark the $T = 0$ Minkowskian results of Refs. [35] and [36] obtained within perturbation theory at one loop. We calculate the integrals of the sigma self-energy both in Euclidean and Minkowski spaces with the renormalization prescription of Ref. [35] and then carry out the analytic continuation (cf. Ch. 6.3 of Ref. [37]) of the Euclidean bubble integrals using Padé approximants. We construct one Padé approximant for each bubble integral, as it turns out that with this procedure we get better agreement with the Minkowskian results than in the case where a single Padé approximant is associated to the entire Euclidean self-energy.

The physically relevant complex pole of the sigma propagator is on the second Riemann sheet (see e.g. Sec. 1.3 of Ref. [38]), which is accessed by crossing the real axis in between the thresholds of the pion and the sigma bubbles. In the present case, this range is given in terms of the tree-level pion and sigma masses as $\sqrt{s} \in [2m_{\pi,0}, 2m_{\sigma,0}]$.

In the search for the complex pole of the σ propagator, we continue the Padé approximant (21) to complex values of its argument. With the parameters given in the first line of Table I in Ref. [35], we find a complex pole at $\sqrt{s} = 569.25 - i \cdot 119.02$ MeV, using the exact formulas of the bubbles analytically continued to the second Riemann sheet, and at $\sqrt{s} = 569.32 - i \cdot 118.83$ MeV, using the multipoint Padé approximation with $N = 200$ points in the [0,3] GeV interval of Euclidean momentum. This finding is in line with the low temperature location of pole II in the second Riemann sheet shown in Fig. 6 of Ref. [36].[7] As in Fig. 3 of Ref. [39], the real part of this pole is close to the maximum of the spectral function, which is accurately reproduced with a Padé approximant using $N = 200$ points, in line with the findings of the previous subsection. However, a word of caution is in order, since, as we show in Fig. 5, far from the real axis, the contours $\Re G_\sigma^{-1}(\sqrt{s}) = 0$ and $\Im G_\sigma^{-1}(\sqrt{s}) = 0$ are strongly distorted. This is because the Padé approximants, fitted to the bubble integrals, being rational functions, induce spurious poles in the propagator. In the shown range, there are eight fake poles, four to the left and four to the right of the physical one. We observed that the number of fake poles within this range stayed constant as we increased N from 200 to 1000, but their position varied significantly compared to that of the physical pole. While in our benchmark case we are lucky, as the position of the physical pole is well captured with the Padé analytic continuation, one should always check whether the result obtained in the complex plane is influenced by nonphysical poles of the Padé approximant.

The fact that the Padé analytic continuation gives so accurately the coordinates of a complex pole on the second Riemann sheet located far away from the real axis is a surprise to us in view of the fact that, as already mentioned, the Padé approximant does not know about the existence of different Riemann sheets. When using Padé approximants, one can in principle mimic to some extent the procedure of the analytic continuation based on a known functional

[7]However, we could not reproduce the results shown in Fig. 2 of Ref. [39], where the scale of the imaginary axis seems to be off.

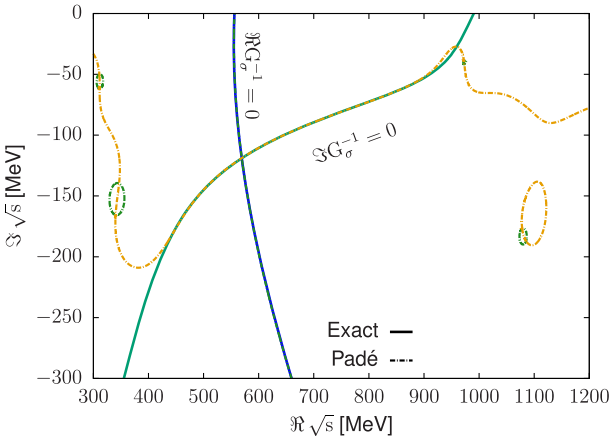

FIG. 5. The zero contours of the real and imaginary parts of the inverse σ propagator given by analytic expression on the second Riemann sheet compared to the corresponding quantities obtained using multipoint Padé approximation with $N = 200$ points. The physical pole is well reproduced, although the Padé approximation gives additionally eight spurious poles in the shown range.

form. In order to do this, we continue the Euclidean bubbles to the real axis, and then we construct new Padé approximants for the real and imaginary parts of the pion bubble for $\sqrt{s} > 2m_{\pi,0}$ and a new Padé approximant for the sigma self-energy in the range $\sqrt{s} \in [2m_{\pi,0}, 2m_{\sigma,0}]$ where it is purely real. One can then continue these Padé approximants to complex values. Actually, Fig. 5 was obtained in this way, and in the present case, no significant change in the coordinates of the complex pole and of the zero contours was observed for $\Re\sqrt{s} < 2m_{\sigma,0}$.

Recently, a Padé approximant of a different form than the one given in Eq. (21) was used in Refs. [40,41] for the analytic continuation into the second Riemann sheet of the $\pi\pi$ scattering amplitude in the scalar-isoscalar ($I = J = 0$) and vector-isovector ($I = J = 1$) channels parametrized in terms of the corresponding phase shifts measured experimentally at low energy values ($\sqrt{s}$). In these references, the location of the σ ($f_0(500)$) and ρ complex poles was determined using single-pole Padé approximants $P_1^N(s, s_0)$ with $N = 2$ or $N = 3$ representing the number of derivatives of the amplitude known at s_0. The precision of the pole determination is comparable with that of alternative approaches. The rate of the convergence with increasing N of the position and residue of the pole was studied in Refs. [40,42], while the uncertainties of the pole location to the parametrization of the partial wave were investigated in Ref. [43]. These results suggest that in our case one could try to analytically continue the propagator (and not the self-energy) from real to complex values of $\sqrt{s}$ using a $P_1^N(s, s_0)$ Padé approximant. This will exclude the fake poles encountered in Fig. 5, possibly at the expense of a less accurate determination of the complex pole position compared to the case when the multipoint Padé approximation is used.

IV. COMPARISON OF POLE AND ZERO-MOMENTUM MASSES IN THE $O(N)$ MODEL

In our earlier works [21,22], we have studied the parametrization of the $O(4)$ model in regard to its application to light meson phenomenology. The parametrization was done using zero-momentum masses for simplicity. However, a correct parametrization requires, instead, the use of pole masses. Here, we use the Padé analytic continuation method in order to assess how different these masses can be. We should mention that this comparison only makes sense in a given renormalization scheme because the zero-momentum masses are scheme dependent whereas the pole masses are not.

Another subtlety comes from the fact that, in a given 2PI approximation, one can define two types of propagators, the so-called internal and external propagators. The internal propagator is the one considered in Sec. II for the case of the two-loop approximation. However, one can define an external propagator, as we recall in the next subsection. Since the parametrization of Refs. [21,22] was done using the zero-momentum mass of the external propagator, in what follows, we compare this mass with the pole mass of the same propagator. In doing so, we shall use a well-motivated approximation for the external propagator which leads to the same expression in the two-loop and $\mathcal{O}(\lambda^2)$ truncations of the 2PI effective action, the two approximations used in Refs. [21,22]. For completeness, we shall also do this comparison in the case of the internal propagators which are different in the two types of truncations.

A. External vs internal propagators

In the 2PI formalism, the internal propagator $\bar{G}_\phi$ in the presence of a given field expectation value is obtained by solving the equation $0 = \delta\Gamma[\phi, G]/\delta G_{G=\bar{G}_\phi}$, where $\Gamma[\phi, G]$ is the so-called 2PI effective action. Knowing $\bar{G}_\phi$, one can reconstruct the usual one-particle irreducible (1PI) effective action as $\Gamma[\phi] = \Gamma[\phi, \bar{G}_\phi]$. From the latter, it is also possible to compute the propagator as $\mathcal{G}^{-1} = \delta^2\Gamma/\delta\phi^2$. Although these two definitions for the two-point function are equivalent in the absence of approximations, they differ in practice whenever a truncation of $\Gamma[\phi, G]$ is considered, and the second definition is referred to as the external propagator. We refer to Ref. [26] for details on the relation between the two types of propagators and their respective renormalization. Here, we recall the expression for the external propagator in the two-loop and $\mathcal{O}(\lambda^2)$ truncations, in the $N = 1$ case. In Euclidean configuration space, one obtains

$$\mathcal{G}_{\mathrm{E}}^{-1}(x, y) = \left.\frac{\delta^2\Gamma[\phi, G]}{\delta\phi(x)\delta\phi(y)}\right|_{G=\bar{G}_\phi} - \frac{1}{2}\int_{z_1,z_2,z_3,z_4} \Lambda(x; z_1, z_2) \times \bar{G}_{\mathrm{E}}(z_1, z_3)\bar{G}_{\mathrm{E}}(z_4, z_2)V(z_3, z_4; y), \quad (25)$$

with

$$\left.\frac{\delta^2\Gamma[\phi,G]}{\delta\phi(x)\delta\phi(y)}\right|_{G=\bar{G}_\phi} = \mathcal{G}^{-1}_{\mathrm{E},0}(x-y) - \frac{\lambda^2}{6}\bar{G}^3_{\mathrm{E}}(x-y) + \frac{1}{2}[\lambda_4\phi^2 + \lambda_2\bar{G}_{\mathrm{E}}(0)]\delta(x-y), \quad (26)$$

where we have restricted to homogeneous fields $\phi(x) = \phi$ and where $\Lambda(x; z_1, z_2)$ and $V(z_1, z_2; x)$ are proportional to ϕ and have tree-level contributions equal to $\lambda_2\phi\delta(x - z_1)\delta(x - z_2)$. In this work, we shall neglect all contributions to Λ and V beyond tree level, which is the minimum needed if we want the two-loop external propagator to contain at least the same diagrams as the two-loop internal one. Higher order contributions, since they are proportional to ϕ^2, lead only to logarithmic modifications of the momentum dependence of the self-energy. We thus expect those contributions not to modify by much the values of the pole and zero-momentum masses. This is an important simplification because, in general, obtaining the function V requires solving a Bethe-Salpeter equation, which we avoid here without affecting our conclusions in a dramatic way. Putting these pieces together and Fourier transforming, we arrive at $\mathcal{G}^{-1}_{\mathrm{E}}(Q_{\mathrm{E}}) \equiv Q^2_{\mathrm{E}} + \hat{M}^2_{\mathrm{E}}(Q_{\mathrm{E}})$, with

$$\hat{M}^2_{\mathrm{E}}(Q_{\mathrm{E}}) = \delta Z_2 Q^2_{\mathrm{E}} + m_2^2 + \frac{\lambda_4}{2}\phi^2 + \frac{\lambda_2}{2}\mathcal{T}_{\mathrm{E}}[\bar{G}_{\mathrm{E}}] - \frac{\lambda^2}{2}\phi^2\mathcal{B}[\bar{G}_{\mathrm{E}}](Q_{\mathrm{E}}) - \frac{\lambda^2}{6}\mathcal{S}_{\mathrm{E}}[\bar{G}_{\mathrm{E}}](Q_{\mathrm{E}}). \quad (27)$$

We mention that, in the $\mathcal{O}(\lambda^2)$ truncation, the internal propagator has exactly the same expression as the approximate external propagator introduced above, since the gap mass $\bar{M}^2_{\mathrm{E}}(Q)$ is given by the right-hand side of (27).

In fact, we can do a little bit better concerning the external propagator, as the zero-momentum value $\hat{M}^2_{\mathrm{E}} \equiv \hat{M}^2_{\mathrm{E}}(Q_{\mathrm{E}} = 0)$ does not need to be approximated but can be computed instead from the curvature of the effective potential associated to the effective action. Proceeding this way, one completely takes into account the contribution of the Bethe-Salpeter equation to $\hat{M}^2_{\mathrm{E}}$, and away from $Q_{\mathrm{E}} = 0$, we can approximate $\hat{M}^2_{\mathrm{E}}(Q_{\mathrm{E}})$ by

$$\hat{M}^2_{\mathrm{E}}(Q_{\mathrm{E}}) = \delta Z_2 Q^2_{\mathrm{E}} + \hat{M}^2_{\mathrm{E}} - \frac{\lambda^2}{2}\phi^2[\mathcal{B}[\bar{G}_{\mathrm{E}}](Q_{\mathrm{E}}) - \mathcal{B}[\bar{G}_{\mathrm{E}}]] - \frac{\lambda^2}{6}[\mathcal{S}_{\mathrm{E}}[\bar{G}_{\mathrm{E}}](Q_{\mathrm{E}}) - \mathcal{S}_{\mathrm{E}}[\bar{G}_{\mathrm{E}}]]. \quad (28)$$

The counterterm δZ_2 is needed to absorb divergences in the difference of setting-sun integrals and is determined numerically as explained in Appendix A. 2 of Ref. [22], using instead of $T_\star$ a small value of the temperature, $T = 0.05T_\star$. If we denote by $\hat{M}^2(Q)$ the analytic continuation of $\hat{M}^2_{\mathrm{E}}(Q_{\mathrm{E}})$, the pole mass of the external propagator corresponds to $\hat{M}^2_{\mathrm{p}} = \hat{M}^2(\hat{M}^2_{\mathrm{p}})$.

The generalization of Eq. (28) to the $O(4)$ case is straightforward. To get the approximated $\hat{M}^2_{\mathrm{L,E}}(Q)$ and $\hat{M}^2_{\mathrm{T,E}}(Q)$ in the corresponding longitudinal and transverse external propagators, one can use the expressions given in Eq. (15) of Ref. [22], subtract from the right-hand side the zero-momentum expression, and add the corresponding curvature mass determined numerically using Eq. (16) of that reference. We emphasize that the approximated expressions are the same in the two-loop and $\mathcal{O}(\lambda^2)$ truncations, but the internal propagators entering the integrals are different in the two cases.

B. Quality of the curvature mass-based parametrization of the O(4) model

We now turn to the analytic continuation of the $N = 4$ Euclidean results obtained in Refs. [21,22] at a small value of the temperature, $T = 0.05T_\star$. Applying the method based on Padé approximants, we find similar results in the two investigated truncations for any parameters where the curvature masses (zero-momentum masses of the external propagator) are physical. The main result is that, although the difference between the pole masses of the longitudinal external and internal propagators can be of 40%, the difference between the pole and zero-momentum mass of a given propagator (internal or external) is only within 1%. For the transverse mode, the differences are typically smaller, which is in line with the results of Refs. [13,23] obtained using the FRG approach. We already knew from previous studies that the difference between $\hat{M}_{\mathrm{L}}$ and $\bar{M}_{\mathrm{L}}$ could be more than 30% for some parameters (see Fig. 3 of Ref. [22]), and now we see that both $\bar{M}_{\mathrm{L/T}} - \bar{M}_{\mathrm{L/T,p}}$ and $\hat{M}_{\mathrm{L/T}} - \hat{M}_{\mathrm{L/T,p}}$ are very small in both truncations, for parameters where the curvature masses are physical. For such parameters, the pole of the analytically continued sigma propagator becomes complex. Based on the study presented in Sec. III. B, we interpret this pole as being the physical pole on the second Riemann sheet. Unfortunately, the imaginary part of the pole is almost zero; the ratio between real and imaginary part is $\sim 10^{-3}$. We illustrate this for a typical parameter set of the two-loop truncation in Fig. 6, where the plots are obtained by continuing the Euclidean external longitudinal propagator calculated with the approximation described above.

The smallness of the imaginary part of the complex σ pole is in line with the findings of Ref. [44], where it turned out that at leading order in a $1/N$ expansion its ratio to the real part of the pole only starts to grow for larger values of the coupling and becomes physically acceptable for $\lambda \in (300, 400)$. We mention that, taking into account the scaling by $N = 4$ used in Refs. [21,22], the coupling of Ref. [35] (also used in Sec. III. B) corresponds to $\lambda = 292$. Even for such a big value of the coupling constant, $M_{\mathrm{L}}(Q = 0)$ is only 1.7% larger than $M_{\mathrm{L,p}}$ given in

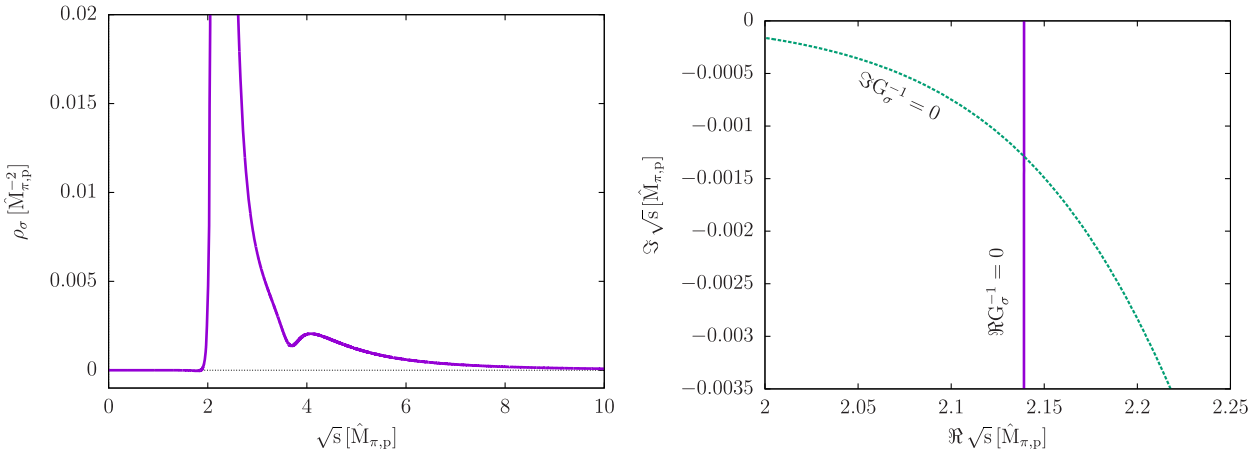

FIG. 6. The result of the analytic continuation of Euclidean data for the external propagator obtained with a two-loop truncation for a typical parameter set ($m^2 = 0.23, \lambda = 28.257, h = 0.62$). Left panel: the spectral function in the sigma channel. Right panel: the zero-contour lines of the real and imaginary parts of the inverse σ propagator showing the complex sigma pole with a very small imaginary part.

Sec. III. B. Such a large value of the coupling, which is by a factor of 5 larger than the largest coupling used for parametrization in Refs. [21,22], cannot be reached in our 2PI investigations because the closeness of the Landau pole to the physical scales makes the solution of the propagator equation, if accessible at all iteratively, highly cutoff sensitive.

C. Infrared sensitivity of the pole mass in the two-loop SI2PI approximation

In Ref. [25], we investigated the SI2PI formalism of Ref. [24] at two-loop order, using various types of UV regulators. In particular, we pointed out that, for generic smooth regulators, the solution for the internal propagator of the SI2PI framework possesses an untamed infrared sensitivity in the broken phase that leads to a loss of solution for large enough volumes. This may not be a problem, though, in cases in which the volume at which the solution disappears is many order of magnitudes higher than the physical volume of the system under study and in which the quantity under scrutiny presents a *plateau* behavior for a large range of volumes below the volume at which the solution is lost. In Ref. [25], we tested this scenario on the zero-momentum mass of the Higgs propagator in the model of Ref. [24], and we observed sensible changes with the volume as we also illustrate in Fig. 7. However, as pointed out to us by D. Teresi, in the same model, the Higgs pole mass should be (almost) insensitive to the volume. This insensitivity was reported in Ref. [45], and it is expected based on the fact that the Higgs pole mass is not related to the zero-momentum behavior of the propagator, which is the only region where the propagator is infrared sensitive in our case. However, we note that it is not clear which type of UV regulator was used in Refs. [24,45], so one could *a priori* think that the insensitivity could also originate from the use of a sharp regulator that tames artificially the IR sensitivity, as explained in Ref. [25].

We can now test these scenarios using the Padé continuation technique with various types of UV regulators. The result for the Higgs pole mass is compared to the zero-momentum Higgs mass in Fig. 7. Imposing the constraint of the SI2PI formalism as $\bar{M}_{\mathrm{T}}(|K_{\mathrm{E}}| = \kappa) = 0$, we observe that, even with a smooth UV regulator, for which the internal Higgs propagator ceases to exist beyond some volume, the corresponding pole shows a plateau behavior over a large range of volumes.

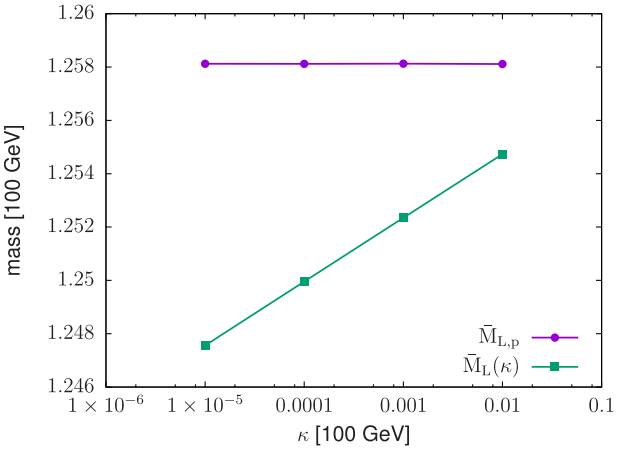

FIG. 7. Infrared sensitivity of the zero-momentum and pole "Higgs" masses in an $O(2)$ model using the symmetry improved 2PI framework. The solution is in principle lost if one insists on removing the infrared regulator κ (which is inversely proportional to the typical linear size of the system). However, before this happens, the pole mass presents a plateau behavior that allows us to define the mass of the particle in a very accurate way. We used the parameters of Ref. [24] and the nonequidistant grid of Ref. [25] with $N_s = 151$ points. All these points in the $\sqrt{s} \in [\kappa, \Lambda]$ range, with $\Lambda = 5$ TeV, were used to construct the Padé approximant.

V. CONCLUSIONS

We searched for broken phase Minkowski space solutions in the (m^2, λ) parameter space of the one-component φ^4 model at zero temperature using the 2PI effective action truncated at two-loop level. Since the Euclidean solution can be obtained from the spectral function, we could use the Minkowskian solution as a benchmark for the analytic continuation of the Euclidean propagator with the method based on multipoint Padé approximants. The various tests we performed show that at zero temperature the Padé analytic continuation is an efficient tool to obtain not only the spectral function but also the complex pole of the propagator on the second Riemann sheet. However, it is expected that, as the temperature grows, the applicability of the method is limited by the decreasing number of available Matsubara modes in a given frequency interval, as we have argued in Sec. III A.

We applied the Padé analytic continuation on previously determined practically zero temperature Euclidean propagators of the $O(4)$ model and studied the relation between the pole and the gap mass at vanishing external momentum of both the internal and external 2PI propagators. We have searched for real poles of the transverse propagator and for complex poles of the longitudinal propagator on the second Riemann sheet. For parameters where the longitudinal curvature mass (gap mass at vanishing external momentum of the external propagator) is physical, the real part of the corresponding pole is within 1% of the curvature mass, both at two-loop and at $\mathcal{O}(\lambda^2)$ level truncations of the 2PI effective action. This shows that the error of the parametrization of Refs. [21] and [22], where the curvature masses were used instead of the pole masses, is smaller than 1%. However, with the parameters determined in these references, the imaginary part of the pole of the longitudinal external propagator turns out to be very small, although it increases with the value of the coupling constant. Unfortunately, the presence of the Landau pole prevents us from accessing regions of the parameter space with larger values of the coupling, as the solution of the model, which is increasingly difficult to find with an iterative method, becomes highly cutoff sensitive.

ACKNOWLEDGMENTS

We would like to thank D. Teresi for clarifying discussions about his work that motivated the analysis presented in Sec. IV C. In the case of G. M., this work is part of Project No. 121064 for which support was provided by the National Research, Development and Innovation Fund of Hungary, financed under the PD_16 funding scheme. Zs. Sz. would like to thank École Polytechnique for hospitality and support during the last stages of this work.

APPENDIX A: RENORMALIZATION

As mentioned in the Introduction above Eq. (6), we now discuss how to obtain the counterterms with a renormalization at $T = 0$, in a way that resembles the renormalization prescriptions at $T = T_\star$ which were used in some of our previous works. Since there is no physical renormalization condition giving exactly the counterterms determined in Ref. [27], we define m_0^2 and m_2^2 by absorbing those quadratic and logarithmic divergences which arise when expanding the propagator $\bar{G}$ around $G_0(Q) = i/(Q^2 - M_0^2 + i\varepsilon)$ and do not depend on the environment (ϕ or $\mathcal{T}_{\rm F}[\bar{G}]$). One has

$$m_0^2 = m^2 - \frac{\lambda_0}{2}\mathcal{T}_{\rm div}[\bar{G}], \tag{A1}$$

$$m_2^2 = m^2 - \frac{\lambda_0}{2}\mathcal{T}_{\rm div}[\bar{G}] - \frac{\lambda^2}{6}\mathcal{S}_{\rm div}[\bar{G}], \tag{A2}$$

where the environmental free divergences of the tadpole and setting-sun integrals are given by

$$\mathcal{T}_{\rm div}[\bar{G}] = \mathcal{T}[G_0] + (m^2 - M_0^2)\mathcal{I}[G_0], \tag{A3}$$

$$\mathcal{S}_{\rm div}[\bar{G}] = \mathcal{S}[G_0] + 3(m^2 - M_0^2)[T_{\rm d}^{(I)} + \mathcal{I}^2[G_0]], \tag{A4}$$

with $T_{\rm d}^{(I)} = -i\int_Q G_0^2(Q)\mathcal{I}_{\rm F}[G_0](Q)$.

In order to renormalize the couplings, we proceed as usual at $\phi = 0$ (see Ref. [26] for details) and introduce the 2PI kernels and the related four-point functions but formally replace in them, and in the equations they satisfy, $\bar{G}_{\phi=0}$ by G_0. One has for instance

$$\bar{V}_0 = \bar{\Lambda}_0 + \frac{1}{2}\bar{V}_0\bar{\Lambda}_0\mathcal{I}[G_0], \tag{A5}$$

$$V_0(0,K) = \Lambda_0(0,K) - \frac{i}{2}\int_Q \Lambda_0(0,Q)G_0^2(Q)\bar{V}_0, \tag{A6}$$

where at the present order of truncation

$$\bar{\Lambda}_0 \equiv 4\frac{\delta^2\gamma_{\rm int}}{\delta G\delta G}\bigg|_{\phi=0,G_{\phi=0}\to G_0} = \lambda_0, \tag{A7}$$

$$\Lambda_0(0,K) \equiv 2\frac{\delta^3\gamma_{\rm int}}{\delta\phi\delta\phi\delta G(K)}\bigg|_{\phi=0,G_{\phi=0}\to G_0} = \lambda_2 + \lambda^2\mathcal{I}[G_0](K). \tag{A8}$$

λ_0 is obtained from the condition $\bar{V}_0 = \lambda$ in the form $\lambda_0^{-1} = \lambda^{-1} + \mathcal{I}[G_0]/2$, while λ_2 is obtained from the condition $V_0(0,K) = \lambda$, which gives after a few lines of algebra $\lambda_2 = \lambda_0 - \lambda^2\mathcal{I}[G_0] - \lambda^2\lambda_0 T_{\rm d}^{(I)}/2$. The counterterm $\delta\lambda_4$ is obtained from the condition $\hat{V}_0 = \lambda$, using the equation for

$$\hat{V}_0 \equiv \frac{\delta^4\gamma}{\delta\phi^4}\bigg|_{\phi=0,G_{\phi=0}\to G_0}. \tag{A9}$$

APPENDIX B: DISPERSION RELATIONS AND SOME USEFUL EXPRESSIONS

Let us start by recalling here Eqs. (9) and (10), which can be understood from the sole assumption of the existence of an analytic propagator $\mathcal{G}(Q^2)$ for complex values of Q^2 away from the positive real axis (in the first Riemann sheet), that decreases as $1/Q^2$ at large Q^2 and which gives back the Minkowski propagator when approaching the positive real axis: $G(Q) = \mathcal{G}(Q^2 + i\epsilon)$ with $Q^2 > 0$. Indeed, with the propagator $\mathcal{G}(Q^2)$ being analytic away from the positive real axis, one can apply the Cauchy formula to a small circle not intersecting this axis and centered around a certain Q^2. Deforming this contour into a large circle C_R of which the radius R tends to infinity and a contour B_R with two parallel branches on each side and close to the positive real axis, one obtains

$$\mathcal{G}(Q^2) = \int_{C_R} \frac{ds}{2\pi i} \frac{\mathcal{G}(s)}{s - Q^2} + \int_0^R \frac{ds}{2\pi i} \frac{\mathcal{G}(s + i\epsilon) - \mathcal{G}(s - i\epsilon)}{s - Q^2}. \tag{B1}$$

Owing to the assumed behavior of $\mathcal{G}(s)$ at large s, the first term goes to 0 as $R \to \infty$. The second term can be expressed in terms of the spectral function, and we finally obtain

$$\mathcal{G}(Q) \equiv \int_0^\infty \frac{ds}{2\pi} \frac{i\rho(s)}{Q^2 - s}, \tag{B2}$$

which provides a spectral representation for the analytic propagator that leads to Eq. (9) when approaching the positive real axis. The sum rule is obtained in a similar fashion by applying the argument to the function $(s - Q^2)\mathcal{G}(s)$ instead of $\mathcal{G}(s)$. In this case, the integral over the contour C_R does not vanish and gives the 1 in the right-hand side of Eq. (10).

The previous argument can be repeated for any function $\mathcal{F}(Q^2)$ analytic in Q^2 away from the positive real axis. In the case where $\mathcal{F}(s)$ does not go to zero fast enough, one should apply the argument to $\mathcal{F}(s) - \sum_{p=0}^{n} \mathcal{F}^{(p)}(s_0)(s - s_0)^p/p!$ with n high enough, such that the integral over C_R vanishes as $R \to \infty$. For instance, if $\mathcal{F}(s)$ grows logarithmically, we apply the argument to $\mathcal{F}(s) - \mathcal{F}(s_0)$ with $s_0 = Q_0^2$ away from the positive real axis. We obtain, for any Q^2 and Q_0^2 away from the positive real axis,

$$\mathcal{F}(Q^2) - \mathcal{F}(Q_0^2) = \int_0^\infty \frac{ds}{\pi} \frac{(Q^2 - Q_0^2)\Im F(s)}{(s - Q^2)(s - Q_0^2)}. \tag{B3}$$

In particular, if one is interested in $F(Q) \equiv \mathcal{F}(Q^2 + i\epsilon)$, one has for Q^2 and Q_0^2 real,

$$F(Q) - F(Q_0) = \int_0^\infty \frac{ds}{\pi} \frac{(Q^2 - Q_0^2)\Im F(s)}{(s - Q^2 - i\epsilon)(s - Q_0^2 - i\epsilon)}. \tag{B4}$$

The previous formula applies in particular to the finite bubble integral considered in the present work. Indeed, using the spectral representation and its sum rule,

$$\mathcal{I}_F[G](Q) = \int_0^\infty \frac{ds_1}{2\pi} \int_0^\infty \frac{ds_2}{2\pi} \rho(s_1)\rho(s_2)\mathcal{I}_{0,\mathrm{F}}[G_1, G_2](Q), \tag{B5}$$

from which it follows that this is analytic in the variable Q^2 away from the positive real axis. Moreover, since the finite bubble grows like $\ln Q^2$, we need to apply the once-subtracted formula.

Let us now derive some other useful results [8]. We start from the identity $\bar{G}(Q)\bar{G}^{-1}(Q) = 1$ and derive two expressions for the finite wave-function renormalization constant Z, the expression for the continuum part of the spectral function and the sum rule it satisfies. For $\bar{G}(Q)$, we use its spectral representation (9), while for the inverse propagator, we use the expression $\bar{G}^{-1}(Q) = -i(Q^2 - \bar{M}^2(Q) + i\epsilon)$. The gap mass is a complex valued function, and $\Re\bar{M}^2(Q)$ and $\Im\bar{M}^2(Q)$ can be read off from (6a), remembering that only the bubble integral has an imaginary part. Using the form of the spectral function given in (16) and the relation

$$\frac{1}{Q^2 - s + i\varepsilon} = \mathcal{P}\frac{1}{Q^2 - s} - i\pi\delta(Q^2 - s), \tag{B6}$$

one obtains from $GG^{-1} = 1$ two equations, one for the real part and one for the imaginary part. With some algebraic manipulations, one derives from them the usual expression for the continuum part of the spectral function

$$\sigma(Q^2) = -2\frac{\Im\bar{M}^2(Q)}{(Q^2 - \Re\bar{M}^2(Q))^2 + (\Im\bar{M}^2(Q))^2} \tag{B7}$$

and the equation ($s_{\mathrm{th}} = 4\bar{M}_{\mathrm{p}}^2$)

$$Z + (Q^2 - \bar{M}_{\mathrm{p}}^2)\mathcal{P}\int_{s_{\mathrm{th}}}^\infty \frac{ds}{2\pi}\frac{\sigma(s)}{Q^2 - s} = \frac{(Q^2 - \bar{M}_{\mathrm{p}}^2)(Q^2 - \Re\bar{M}^2(Q))^2}{(Q^2 - \Re\bar{M}^2(Q))^2 + (\Im\bar{M}^2(Q))^2}. \tag{B8}$$

Taking the limit $Q \to \infty$ in (B8), one obtains

$$Z + \int_{s_{\mathrm{th}}}^\infty \frac{ds}{2\pi}\sigma(s) = 1, \tag{B9}$$

which is the sum rule for a spectral function of the form (16), while taking the limit $Q \to \bar{M}_{\mathrm{p}}$, one obtains

$$Z = \left(1 - \frac{d\Re\bar{M}^2(Q)}{dQ}\bigg|_{Q=\bar{M}_{\rm p}}\right)^{-1}, \tag{B10}$$

which is the residue of the pole $Q = \bar{M}_{\rm p}$ of the propagator.

APPENDIX C: NUMERICAL ALGORITHM AND ITS IMPLEMENTATION

In this Appendix, we describe the steps of the iterative process applied to solve sequentially the explicitly finite coupled field and gap Eqs. (6) and present the numerical implementation of these steps.

Being interested in broken symmetry phase solutions, we start from an initial propagator $\bar{G}^{(0)}$ and express the nontrivial $(\bar{\phi}^2)^{(1)}$ from the field equation. Then, using both $\bar{\phi}^{(1)}$ and $\bar{G}^{(0)}$, we evaluate $(\bar{M}^2)^{(1)}$ from (6a), which in turn gives us $\bar{G}^{(1)}(Q)$. These steps are repeated until the relative change from one iteration to the next of both $\bar{\phi}$ and the pole mass $\bar{M}^2_{\rm p}$ obtained from (17) is less than our stopping parameter, chosen to be 10^{-7}. If $(\bar{\phi}^2)^{(i+1)} < 0$, we leave $\bar{\phi}^{(i+1)} = \bar{\phi}^{(i)}$. When for five consecutive iterative steps $\bar{\phi}^2$ is negative, we stop the iteration and say that no broken phase solution was found for the given parameters and/or initial values.

The explicit steps for one full iteration (from the ith to $i+1$th) are the following; the propagator $G^{(i)}$ is used to denote a given quantity in the ith iteration, even though it is clear from Sec. II B that the spectral function of the form (16) is the central object of the entire iterative procedure:

(i) Using (7) and (8), evaluate $\mathcal{S}_{\rm F}[\bar{G}^{(i)}_{\rm E}]$ and $\mathcal{T}_{\rm F}[\bar{G}^{(i)}_{\rm E}]$, and update $\bar{\phi}^{(i+1)}$ from (6b).

(ii) Evaluate $\Im\mathcal{I}[\bar{G}^{(i)}](Q)$ using (11) and then $\Re\mathcal{I}_{\rm F}[\bar{G}^{(i)}](Q)$ using the dispersion relation (18).

(iii) Determine $(\bar{M}^2_{\rm p})^{(i+1)}$ solving the pole Eq. (17) and update $\sigma^{(i+1)}(s)$ using its expression given in (B7); then, update Z using the sum rule (B9).[8]

We initialize $\bar{\phi}$ with some crude nonzero estimate of the solution (e.g. the classical value $\sqrt{-m^2/\lambda}$) and choose the initial spectral function to contain only a pole part with unit residue, with the pole at $\bar{M}_{\rm H}$, defined as the solution of the gap equation in the Hartree approximation

$$\bar{M}^2_{\rm H} = m^2 + \frac{\lambda}{2}(\bar{\phi}^2 + \mathcal{T}_{\rm F}[\bar{G}_{\rm H}]), \tag{C1}$$

with $\bar{G}_{\rm H}(Q) = i/(Q^2 - \bar{M}^2_{\rm H} + i\varepsilon)$.

We note that one can introduce a reparametrization of the Eqs. (6) in terms of the mass parameter

$$M^2 = \bar{M}^2_{\phi=\bar{\phi}}(Q=0), \tag{C2}$$

that is the zero-momentum value of the self-energy. While this introduces some intricacy connected to the fact that M^2 depends on the *a priori* unknown solution $\bar{\phi}$, it has several advantages. First, by fixing the local part of the self-energy, the number of iterations required for convergence is greatly reduced. Also, the tadpole diagram (2), one of the main sources of numerical error, only has to be evaluated to obtain m^2 corresponding to the fixed value of M^2. Second, this allows the introduction of an under-relaxation parameter α as

$$(\bar{\phi}^{(i+1)}_\alpha)^2 = \alpha(\bar{\phi}^{(i+1)})^2 + (1-\alpha)(\bar{\phi}^{(i)})^2. \tag{C3}$$

This is needed to achieve convergence in parameter regions where otherwise our iterative method fails. This, combined with the good initial guess provided by M^2, allowed us to find the unphysical solution shown in Fig. 2.

1. Numerical implementation

In the iterative method described above, we have to store $\bar{\phi}$, $\bar{M}^2_{\rm p}$, and a discretized version of $\sigma(s)$. For the latter, we use a grid of N_s points (typically, we use $N_s = 500$) defined actually in the transformed variable $t = \frac{s}{1+s}$. Starting from $t(s = s_{\rm th})$ and ending in 1, one has

$$t_i = \kappa + i^3 \times \Delta, \qquad i = 0 \ldots N_s - 1, \tag{C4}$$

with $\kappa = \frac{s_{\rm th}}{s_{\rm th}+1}$ and $\Delta = \frac{1-\kappa}{(N_s-1)^3}$. The property $t(s=\infty) = 1$ allows us to carry out the s-integrals of Sec. II B without introducing an explicit numerical cutoff.

We follow below the order of the iterative steps described above and give some technical details concerning the evaluation of the integrals.

The explicitly finite expression of the two local Euclidean integrals, the tadpole $\mathcal{T}_{\rm F}[\bar{G}_{\rm E}]$ and $\mathcal{S}_{\rm F}[\bar{G}_{\rm E}]$, is given in Appendix D, in (D1) and (D2)–(D3), respectively, in terms of the Euclidean propagator (19). The integral of (19) is evaluated on a rather complicated-looking momentum grid defined as

$$q_i = i^{\alpha(i)} \times \Delta(i), \qquad i = 0 \ldots N_s - 1,$$
$$\alpha(i) = 2 + \frac{2}{\pi}\operatorname{atan}\left(\sinh\left(5 - \frac{10i}{N_s - 1}\right)\right), \tag{C5}$$

with $\Delta(i) = \Lambda/(N_s-1)^{\alpha(i)}$, where Λ is an appropriate numerical cutoff for which we typically use values in the range (50–200).[9] The reason for using such a grid is to sample with sufficient accuracy the Euclidean propagator in both the IR and UV regions. For integration, we need to know $G_{\rm E}$ in

[8] Note that, by changing $\bar{M}^2_{\rm p}$ in each iteration, $s_{\rm th}$ also changes. Due to the structure of the bubble integral, $(s_{\rm th})^{(i+1)} = 4(\bar{M}^2_{\rm p})^{(i)}$.

[9] In principle, we could also use a transformed variable similar to (C4) and integrate up to infinity since the integrals are finite. However, the integrands of (D1) and (D2)–(D3) only decrease fast enough due to cancellations, which break down when numerical number representation errors are comparable to the results.

between the grid points, but in order to improve on the UV behavior, we subtract $1/(q_i^2 + M_0^2)$ from $G_{\mathrm{E}}(q_i)$ and fit the difference with a Steffen spline.[10] This proves to be accurate enough in the UV to see the apparent convergence of the integrals with increasing Λ. The spline is evaluated in the integrand called by the CQUAD adaptive integration routine of Gnu Scientic Library (GSL) library [46].

To compute $\Im\mathcal{I}[\bar{G}](Q)$, we use (16) in (11). This leads to $\delta\times\delta$, $\delta\times\sigma$, and $\sigma\times\sigma$ type terms, which start giving a nonvanishing contribution for $Q > 2\bar{M}_{\mathrm{p}}$, $Q > 3\bar{M}_{\mathrm{p}}$, and $Q > 4\bar{M}_{\mathrm{p}}$, respectively. Since $\Im\mathcal{I}[\bar{G}](Q)$ will be used in the dispersion relation (18) giving $\Re\mathcal{I}_{\mathrm{F}}[\bar{G}](Q)$, we spline it in order to be able to evaluate it anywhere. We use the grid introduced for σ in (C4) in the same transformed coordinates. However, a spline interpolation cannot reproduce a functional form with infinite derivatives, such as $\Im\mathcal{I}[\bar{G}](Q)$, which behaves as a square root function around $Q = 2\bar{M}_{\mathrm{p}}$. Therefore, in order to avoid this problem, we chose to fit with a cubic spline the function $(\Im\mathcal{I}[\bar{G}](Q))^2$.

$\Re\mathcal{I}_{\mathrm{F}}[\bar{G}](Q)$ is evaluated from the dispersion relation (18). In order to circumvent the problem of numerically computing integrals with a principal value prescription when $s = Q^2 > 4\bar{M}_{\mathrm{p}}^2$, we rewrite them with the usual method (see e.g. Ref. [47]). First, we split the interval of integration by introducing the point $2s - 4\bar{M}_{\mathrm{p}}^2$; then, we add and subtract an appropriate term in the integrand of the resulting integral over the interval $[4\bar{M}_{\mathrm{p}}^2, 2s - 4\bar{M}_{\mathrm{p}}^2]$, exploiting the fact that $\mathcal{P}\int_a^{2b-a} dx/(x-b) = 0$. In this way, we obtain

$$\begin{aligned}
&\mathcal{P}\int_{4\bar{M}_{\mathrm{p}}^2}^{\infty} ds' \frac{\Im\mathcal{I}[\bar{G}](\sqrt{s'})}{s'(s'-s)} \\
&= \mathcal{P}\int_{4\bar{M}_{\mathrm{p}}^2}^{2s-4\bar{M}_{\mathrm{p}}^2} \frac{ds'}{s'-s}\left(\frac{\Im\mathcal{I}[\bar{G}](\sqrt{s'})}{s'} - \frac{\Im\mathcal{I}[\bar{G}](\sqrt{s})}{s}\right) \\
&\quad + \int_{2s-4\bar{M}_{\mathrm{p}}^2}^{\infty} ds' \frac{\Im\mathcal{I}[\bar{G}](\sqrt{s'})}{s'(s'-s)}. \qquad \text{(C6)}
\end{aligned}$$

Actually, the integrand of the first integral on the rhs is continuous at $s' = s$, so that the principal value prescription can be omitted when integrating it numerically with the CQUAD routine.

We end this part by mentioning two numerical intricacies. The first is encountered when fitting σ with a spline on the grid (C4). σ grows out at the threshold as a square root function, similarly to $\Im\mathcal{I}[\bar{G}]$. However, contrary to $\Im\mathcal{I}[\bar{G}]$, which enters integrals which decrease fast enough in the UV [see the suppression by powers of s in (C6)], the convergence of the integrals with σ [see e.g. (11) and (B9)] is assured by the UV behavior of σ, which has to be preserved by the fit. This time, fitting σ^2 would not be enough because when computing integrals using the transformed variable t [see the definition in the paragraph before (C4)] the Jacobian $J(t) = (1-t)^{-2}$ of the transformation is divergent as $t \to 1$. This would lead in the integrals involving σ to a blowing-up of the oscillations of the spline when $t \to 1$. Since $\lim_{t\to 1} J(t)\sigma(t)$ is finite, the way out is to fit the function $(J(t)\sigma(t))^2$ with a spline on the grid introduced in (C4). In this way, the spline respects the requirements of having appropriate behaviors around the threshold and in the UV.

[10]This is used because Steffen's method leads to an interpolation function which is monotonic between the given data points.

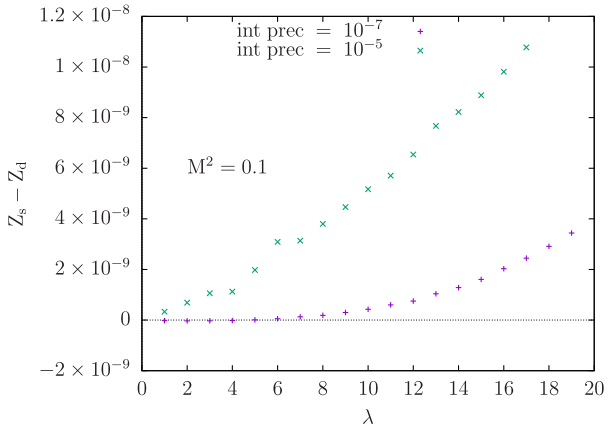

FIG. 8. We show, as a function of the coupling λ, the difference between the two ways of determining the coefficient Z of the singular, pole part of the spectral function: when calculated from (B10) as the residue of the pole, it is denoted by Z_{d}, and when obtained from the sum rule (B9), as done during the iterations, it is denoted by Z_s. See the text for more details.

The second intricacy is related to the coefficient Z of the pole part of the spectral function. This has to be evaluated from iteration to iteration either from the sum rule (B9) or as the residue of the pole (B10). While in principle the two ways of computing Z are equivalent, numerical differences could occur, as we show in Fig. 8. There, we present the value of Z computed in the above-mentioned two ways at the end of the iterative method. It turned out that for the iterations to converge it is actually very important to ensure that the sum rule is satisfied iteration by iteration, since this guarantees the proper asymptotic behavior of the propagator, which was also used to renormalize the real part of the bubble (see Sec. II B). Hence, when solving the equations, Z is always evaluated from the sum rule (B9). The difference seen in Fig. 8 has purely a numerical reason. Increasing the precision of the numerical integration substantially reduces the difference which grows with increasing λ.

APPENDIX D: EXPLICIT FORM OF SOME INTEGRALS

In this Appendix, we give the expression of the finite Euclidean tadpole (7a) and setting-sun (7c) integrals after analytically performing as many of their angular

integrals as possible. The cutoff regularization used is such that an integral involving at least two propagators is invariant with respect to shifts of the loop momenta (see e.g. Appendix D of Ref. [32]). The parts containing $G_{\rm r}$, that is (7a) and the third term of (7c), read ($q = |Q_{\rm E}|$)

$$\mathcal{T}_{\rm F}[G_{\rm E}] = \frac{1}{8\pi^2}\int_0^\Lambda dq q^3 G_{\rm r,E}(q), \tag{D1}$$

$$\int_{Q_{\rm E}} G_{\rm r,E}(Q_{\rm E})\mathcal{B}_{\rm F}[G_{0,\rm E}](Q_{\rm E}) = \frac{1}{8\pi^2}\int_0^\Lambda dq q^3 \mathcal{B}_{\rm F}[G_{0,\rm E}](q) G_{\rm r,E}(q), \tag{D2}$$

where

$$G_{\rm r,E}(q) = \delta G_{\rm E}(q) + \left(M_1^2 - M_0^2 - \frac{\lambda^2}{2}\phi^2 \mathcal{B}_{\rm F}[G_{0,\rm E}](q)\right) G_{0,\rm E}^2(q),$$

with $\delta G_{\rm E}(q) = G_{\rm E}(q) - G_{0,\rm E}(q)$ and $G_{0,\rm E}(q) = (q^2 + M_0^2)^{-1}$. Observing that the other two terms of (7c) can be combined, one obtains

$$\begin{aligned}&\mathcal{S}_{\rm E}[\delta G_{\rm E}] + 3\mathcal{S}_{\rm E}[\delta G_{\rm E};\delta G_{\rm E};G_{0,\rm E}] \\ &= \frac{1}{64\pi^5}\int_0^\Lambda dk k \delta G_{\rm E}(k)\int_0^\Lambda dp p \delta G_{\rm E}(p) \\ &\times \int_{|k-p|}^{\min(\Lambda,k+p)} dq q \sqrt{-\lambda(q^2,k^2,p^2)}\,(G_{\rm E}(q) + 2G_{0,\rm E}(q)),\end{aligned} \tag{D3}$$

with $\lambda(q^2, k^2, p^2)$ defined after (11).

[1] J. Braun, H. Gies, and J. M. Pawlowski, Phys. Lett. B **684**, 262 (2010).
[2] J. Braun, L. Fister, J. M. Pawlowski, and F. Rennecke, Phys. Rev. D **94**, 034016 (2016).
[3] R. Contant and M. Q. Huber, arXiv:1706.00943.
[4] H. Reinhardt, G. Burgio, D. Campagnari, E. Ebadati, J. Heffner, M. Quandt, P. Vastag, and H. Vogt, arXiv:1706.02702.
[5] V. Šauli and J. Adam, Nucl. Phys. **A689**, 467 (2001).
[6] H. Van Hees and J. Knoll, Phys. Rev. D **65**, 105005 (2002).
[7] F. Cooper, B. Mihaila, and J. F. Dawson, Phys. Rev. D **70**, 105008 (2004).
[8] V. Šauli, Few-Body Syst. **39**, 45 (2006).
[9] A. Arrizabalaga and U. Reinosa, Eur. Phys. J. A **31**, 754 (2007).
[10] A. Jakovác, Phys. Rev. D **74**, 085026 (2006).
[11] A. Jakovác, Phys. Rev. D **76**, 125004 (2007).
[12] K. Kamikado, N. Strodthoff, L. von Smekal, and J. Wambach, Eur. Phys. J. C **74**, 2806 (2014).
[13] N. Strodthoff, Phys. Rev. D **95**, 076002 (2017).
[14] M. Jarrell and J. E. Gubernatis, Phys. Rep. **269**, 133 (1996).
[15] Y. Burnier and A. Rothkopf, Phys. Rev. Lett. **111**, 182003 (2013).
[16] S. Kim, P. Petreczky, and A. Rothkopf, Phys. Rev. D **91**, 054511 (2015).
[17] C. S. Fischer, J. M. Pawlowski, A. Rothkopf, and C. A. Welzbacher, arXiv:1705.03207.
[18] M. E. Carrington, W. J. Fu, P. Mikula, and D. Pickering, Phys. Rev. D **89**, 025013 (2014).
[19] H. J. Vidberg and J. W. Serene, J. Low Temp. Phys. **29**, 179 (1977).
[20] G. Fejős and Zs. Szép, Phys. Rev. D **84**, 056001 (2011).
[21] G. Markó, U. Reinosa, and Zs. Szép, Phys. Rev. D **87**, 105001 (2013).
[22] G. Markó, U. Reinosa, and Zs. Szép, Phys. Rev. D **92**, 125035 (2015).
[23] A. J. Helmboldt, J. M. Pawlowski, and N. Strodthoff, Phys. Rev. D **91**, 054010 (2015).
[24] A. Pilaftsis and D. Teresi, Nucl. Phys. **B874**, 594 (2013).
[25] G. Markó, U. Reinosa, and Zs. Szép, Nucl. Phys. **B913**, 405 (2016).
[26] J. Berges, S. Borsányi, U. Reinosa, and J. Serreau, Ann. Phys. (Amsterdam) **320**, 344 (2005).
[27] A. Patkós and Zs. Szép, Nucl. Phys. **A811**, 329 (2008).
[28] G. Markó, U. Reinosa, and Zs. Szép, Phys. Rev. D **86**, 085031 (2012).
[29] J. D. Bjorken and S. D. Drell, *Relativistic Quantum Fields* (McGraw-Hill, New York, 1965).
[30] U. Reinosa and Zs. Szép, Phys. Rev. D **83**, 125026 (2011).
[31] M. Bordag and V. Skalozub, J. Phys. A **34**, 461 (2001).
[32] U. Reinosa and Zs. Szép, Phys. Rev. D **85**, 045034 (2012).
[33] G. A. Baker and J. L. Gammel, *The Padé Approximant in Theoretical Physics* (Academic, New York, 1970).
[34] C. M. Bender and S. A. Orszag, *Advanced Mathematical Methods for Scientists and Engineers I, Asymptotic Methods and Perturbation Theory* (Springer, New York, 1999).
[35] S. Chiku and T. Hatsuda, Phys. Rev. D **58**, 076001 (1998).
[36] Y. Hidaka, O. Morimatsu, T. Nishikawa, and M. Ohtani, Phys. Rev. D **68**, 111901 (2003).
[37] L. S. Brown, *Quantum Field Theory* (Cambridge University Press, Cambridge, England, 1994).
[38] A. M. Badalyan, L. P. Kok, M. I. Polikarpov, and Y. A. Simonov, Phys. Rep. **82**, 31 (1982).
[39] Y. Hidaka, O. Morimatsu, and T. Nishikawa, Phys. Rev. D **67**, 056004 (2003).
[40] P. Masjuan and J. J. Sanz-Cillero, Eur. Phys. J. C **73**, 2594 (2013).
[41] P. Masjuan, J. Ruiz de Elvira, and J. J. Sanz-Cillero, Phys. Rev. D **90**, 097901 (2014).

[42] J. J. Sanz-Cillero, arXiv:1002.3512.
[43] I. Caprini, P. Masjuan, J. Ruiz de Elvira, and J. J. Sanz-Cillero, Phys. Rev. D **93**, 076004 (2016).
[44] A. Patkós, Zs. Szép, and P. Szépfalusy, Phys. Lett. B **537**, 77 (2002).
[45] A. Pilaftsis and D. Teresi, Nucl. Phys. **B920**, 298 (2017).
[46] M. Galasi *et al.*, GSL Reference Manual, http://www.gnu.org/software/gsl.
[47] H. Shima and T. Nakayama, *Higher Mathematics for Physics and Engineering* (Springer-Verlag, Berlin, 2010).